PHYSICAL REVIEW D **86,** 093009 (2012)

Implications of $\mathcal{B}(\mu \to e\gamma)$ and Δa_μ on muonic lepton flavor violating processes

Chun-Khiang Chua

Department of Physics, Chung Yuan Christian University, Chung-Li, Taiwan 320, Republic of China

(Received 23 May 2012; published 7 November 2012)

We study the implications of the experimental results on the $\mu \to e\gamma$ decay rate and the muon anomalous magnetic moment on muonic lepton flavor violating processes, such as $\mu \to 3e$ and $\mu N \to eN$. We use a model-independent approach in this analysis, where these processes are considered to be loop induced by exchanging spin-1/2 and spin-0 particles. We explore two complementary cases—those with no cancellation mechanism in amplitudes and those with an internal (built-in) cancellation mechanism. Our main results are as follows: (a) Bounds from rates are used to constrain parameters, such as coupling constants and masses. These constraints can be easily updated by simple scalings, if the experimental situations change. (b) The muon $g-2$ data favors nonchiral interactions. (c) In $\mu \to 3e$ and $\mu N \to eN$ processes, Z-penguin diagrams may play some role, while box diagram contributions to $\mu \to 3e$ are usually highly constrained. (d) In the first case (without any built-in cancellation mechanism), using the recent $\mu \to e\gamma$ bound, we find that $\mu \to 3e$ and $\mu N \to eN$ rates are usually bounded below the present experimental limits by two to three orders of magnitude in general. Furthermore, by comparing Δa_μ and $\mathcal{B}(\mu \to e\gamma)$ data, the couplings of μ and e are found to be highly hierarchical. Additional suppression mechanisms should be called for. (e) In the second case (with a built-in cancellation mechanism), mixing angles can provide additional suppression factors to satisfy the Δa_μ and $\mathcal{B}(\mu \to e\gamma)$ bounds. While the $\mu \to 3e$ rate remains suppressed, the bounds on $\mu N \to eN$ rates, implied from the latest $\mu \to e\gamma$ bound, can be relaxed significantly and can be just below the present experimental limits.

DOI: 10.1103/PhysRevD.86.093009 PACS numbers: 13.35.Bv, 11.30.Hv

I. INTRODUCTION

Charge lepton flavor violating (LFV) processes are prohibited in the Standard Model (SM) and, hence, are excellent probes of New Physics (NP). Recently the search of $\mu \to e\gamma$ decay was reported by the MEG Collaboration giving [1]

$$\mathcal{B}(\mu^+ \to e^+\gamma) \leq 2.4 \times 10^{-12}. \quad (1)$$

The bound is several times lower than the previous one [2]. This result received a lot of attention (see, for example, Refs. [3–5]). In many New Physics models, this decay mode is closely related to other lepton flavor violating processes, such as $\mu^+ \to e^+e^+e^-$ decays and $\mu^- N \to e^- N$ conversions [6]. The present limits and future experimental sensitivities [1,2,7] of these LFV processes are summarized in Table I. Note that present bounds on μ LFV rates are roughly of similar orders. It will be interesting to see what the implications are of the new $\mathcal{B}(\mu \to e\gamma)$ bound on these LFV processes and the interplay between them.

Since 2001, the muon anomalous magnetic moment remains as a hint of a NP contribution (see, for a review, Ref. [8]). Experimental data deviates from the Standard Model (SM) expectation by more than 3σ [2]:

$$\Delta a_\mu = a_\mu^{\rm exp} - a_\mu^{\rm SM} = (287 \pm 63 \pm 49) \pm 10^{-11}. \quad (2)$$

Since NP contributes to Δa_μ and $\mathcal{B}(\mu^+ \to e^+\gamma)$ through very similar loop diagrams [see Figs. 1(a) and 1(b)], it is useful to compare them at the same time.

The Large Hadron Collider is working well. So far no NP signal is found (see, for example Ref. [9]). Plenty of well-studied NP models or scenarios are ruled out or cornered. Therefore, it will be useful to study the low-energy effect, when the NP scale is still beyond our reach. Given the present status on NP models, we believe that it is worthwhile to use a model-independent approach.

In this work we consider a class of models that induce muon $g-2$ and various muon lepton flavor violating processes, such as $\mu \to e\gamma$, $\mu \to 3e$, and $\mu \to e$ conversions, by exchanging spin-1/2 and spin-0 particles in loop diagrams. We try to see where the present $g-2$ and $\mu \to e\gamma$ experimental results lead us on estimating rates or bounds on various LFV muonic decay modes and the interplay between them. Two cases, which are complementary to each other, are considered. In the first case, there is no built-in cancellation mechanism among amplitudes. The second case is with some built-in mechanism, such as Glashow-Iliopoulos-Maiani (GIM) or super GIM mechanism. These two cases will be compared.

The layout of this paper is as follows. In the next section, the framework is given. Numerical results are presented in Sec. III, where bounds from rates are used to constrain parameters, such as coupling constants and masses. Correlations between different processes are investigated. Discussion and conclusion are given in Secs. IV and V,

TABLE I. Current experimental upper limits and future sensitivities on various muonic LFV processes [1,2,7].

	Current limit	Future sensitivity
$\mathcal{B}(\mu^+ \to e^+\gamma)$	$<2.4 \times 10^{-12}$	10^{-13}
$\mathcal{B}(\mu^+ \to e^+e^+e^-)$	$<1.0 \times 10^{-12}$	10^{-14}–10^{-16}
$\mathcal{B}(\mu^-\mathrm{Ti} \to e^-\mathrm{Ti})$	$<4.3 \times 10^{-12}$	10^{-18}
$\mathcal{B}(\mu^-\mathrm{Au} \to e^-\mathrm{Au})$	$<7 \times 10^{-13}$	10^{-14}–10^{-16}
$\mathcal{B}(\mu^-\mathrm{Al} \to e^-\mathrm{Al})$	...	10^{-16}

respectively. Some formulas and additional information are collected in the Appendixes.

II. FRAMEWORK

In this section, we begin with introducing the Lagrangian of a generic interaction involving leptons, exotic spin-1/2 fermions, and spin-0 bosons. Formulas of processes of interest, discussions on subtleties on the calculation of the Z-penguin amplitude, and explicit expressions of Wilson coefficients will be given subsequently. This section ends after the formulation of the two complementary cases as briefly mentioned in Sec. I.

A. The interacting Lagrangian and diagrams

The Lagrangian of a generic interaction involving leptons (l), exotic spin-1/2 fermions (ψ_n), and spin-0 bosons (ϕ_i) is given by

$$\mathcal{L}_{\rm int} = \bar{\psi}_n(g^{ni}_{lL}P_L + g^{ni}_{lR}P_R)l\phi^*_i + \bar{l}(g^{ni*}_{lL}P_R + g^{ni*}_{lR}P_L)\psi_n\phi_i, \quad (3)$$

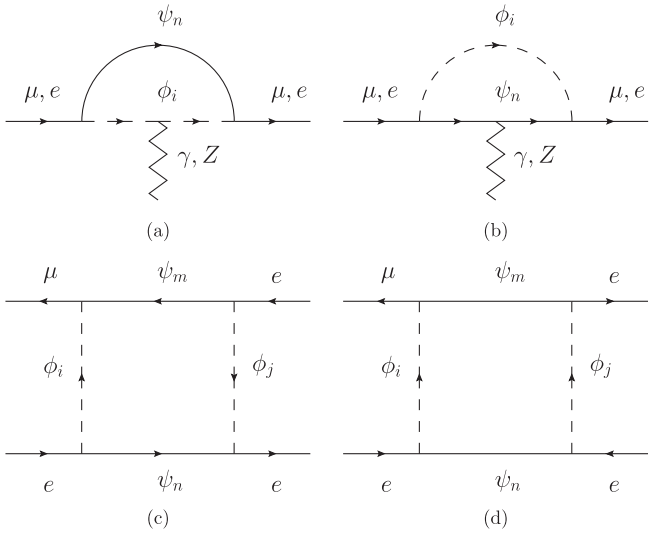

FIG. 1. (a) and (b): Penguin diagrams that contribute to muon $g-2$, $\mu^+ \to e^+\gamma$, $\mu^+ \to e^+e^+e^-$, and $\mu^-N \to e^-N$ processes. Note that diagrams involving self-energy parts are not shown. (c) and (d): Box diagrams contributing to the $\mu^+ \to 3e$ process. Figure (d) takes place only when $\psi_{m,n}$ are Majorana fermions.

where summation over indices is understood unless specified. The Lagrangian is given in the mass bases and is ready to be used in calculations. However, it is important to make sure that it transforms as a singlet under the SM gauge transformation.

In the weak bases of ψ_{Lp}, ψ_{Rp}, ϕ_{La}, and ϕ_{Ra}, the interacting Lagrangian is

$$\mathcal{L}_{\rm int} = (g^{lpa}_{lL}\bar{\psi}_{Rp}l_L\phi^*_{La} + g^{lpa}_{lR}\bar{\psi}_{Lp}l_R\phi^*_{Ra}) + \text{H.c.}, \quad (4)$$

where we denote $\phi_{L(R)}$ for the scalar fields that couple to $l_{L(R)}$ and subscripts p and a are the labels of different weak fields, which may have different SU(2) × U(1) quantum numbers. It is important to require that $\mathcal{L}_{\rm int}$ transforms as a singlet under the SM gauge groups and quantum numbers of ψ and ϕ are related (see Appendix A).

The mass bases are related to the weak bases through the following transformations

$$\phi_i = U^L_{ia}\phi_{La} + U^R_{ia}\phi_{Ra}, \qquad \psi_{nL(R)} = V^{L(R)}_{np}\psi_{L(R)p}, \quad (5)$$

where i and n are labels of mass eigenstates and U and V are the mixing matrices relating weak and mass eigenstates. With

$$g^{ni}_{lL(R)} = g^{lpa}_{lL(R)}V^{R(L)}_{np}U^{L(R)}_{ia} \quad (6)$$

the interacting Lagrangian is now brought into the form shown in Eq. (3), which is more convenient and will be used in later calculations.

These interactions will induce lepton flavor violating processes at the one-loop level. Penguin diagrams contributing to the muon anomalous magnetic moment and $\mu^+ \to e^+\gamma$ are shown in Figs. 1(a) and 1(b), while box diagrams contributing to the $\mu^+ \to 3e$ process are shown in Figs. 1(c) and 1(d). Note that (i) penguin diagrams shown in Figs. 1(a) and 1(b) also contribute to $\mu^+ \to 3e$ and $\mu N \to eN$ processes by connecting the virtual photons or the Z bosons to electron currents and quark currents, respectively,[1] (ii) Fig. 1(d) takes place only when $\psi_{m,n}$ are Majorana fermions.

B. Formulas for various processes

To define our variables and to specify our convention, we collect formulas for various precesses here. The relevant effective Lagrangian in this study is

$$\mathcal{L}_{\rm eff} = \mathcal{L}_{l'l\gamma} + \mathcal{L}_{l'lll} + \mathcal{L}_{l'lqq}, \quad (7)$$

with $l^{(\prime)} = e, \mu, \tau$, and q denoting quarks. Each term will be specified below. For $l' \neq l$, we have

$$\mathcal{L}_{l'l\gamma} = \bar{l}'_L\sigma_{\mu\nu}l_RF^{\mu\nu}A_{L'R} + \bar{l}'_R\sigma_{\mu\nu}l_LF^{\mu\nu}A_{R'L} + \text{H.c.} \quad (8)$$

and

[1]It is possible to have box diagrams with the electron line in Figs. 1(c) and 1(d) replaced by a quark one and contribute to $\mu N \to eN$ conversions in some cases. We will discuss this contribution in the Discussion section.

$$A_{LR'} = A^*_{R'L}, \qquad A_{RL'} = A^*_{L'R}. \tag{9}$$

Note that in the case of $l' = l$, we do not need the additional Hermitian conjugated terms in Eq. (8). These A's are from the so-called F_2 photonic penguin and their explicit forms will be given later.

The effective Lagrangians for $\bar{l}' \to 3l$ decays and $l' \to l$ conversions are [6]

$$\begin{aligned}\mathcal{L}_{l'lll} =& g_{R'LRL}(\bar{l'}_R l_L)(\bar{l}_R l_L) + g_{L'RLR}(\bar{l'}_L l_R)(\bar{l}_L l_R) \\ &+ g_{R'RRR}(\bar{l'}_R \gamma^\mu l_R)(\bar{l}_R \gamma_\mu l_R) + g_{L'LLL}(\bar{l'}_L \gamma^\mu l_L) \\ &\times (\bar{l}_L \gamma_\mu l_L) + g_{R'RLL}(\bar{l'}_R \gamma^\mu l_R)(\bar{l}_L \gamma_\mu l_L) \\ &+ g_{L'LRR}(\bar{l'}_L \gamma^\mu l_L)(\bar{l}_R \gamma_\mu l_R) + \text{H.c.},\end{aligned} \tag{10}$$

$$\begin{aligned}\mathcal{L}_{l'lqq} =& \sum_{q=u,d} [g_{LV}(q)\bar{l'}_L \gamma^\mu l_L + g_{RV}(q)\bar{l'}_R \gamma^\mu l_R]\bar{q}\gamma_\mu q \\ &+ \text{H.c.},\end{aligned} \tag{11}$$

where

$$\begin{aligned} g_{M'MNO} &\equiv e^2 Q_l g^P_{M'M}\delta_{NO} + g^Z_{M'M} g^Z_{l_N}\delta_{NO} + g^B_{M'MNO}, \\ g_{MV}(q) &= eQ^2_q g^P_{M'M} + \frac{1}{2} g^Z_{M'M}(g^Z_{q_L} + g^Z_{q_R}), \end{aligned} \tag{12}$$

for M, N, $O = L$, R with $g^P_{M'M}$ from the so-called F_1 photonic penguin, $g^Z_{M'M}$ from the Z-penguin, and $g^B_{M'MNN}$ from box diagrams. More details and the explicit forms of these Wilson coefficients will be given later. Note that although the above $\mathcal{L}_{l'lqq}$ is not the most generic one, it contains all the relevant parts that are closely related to $\mathcal{L}_{l'lll}$ and $\mathcal{L}_{l'l\gamma}$.

We now collect the formulas for various processes originated from the above Lagrangians. Comparing the effective Lagrangians of the lepton $g-2$ and the electric dipole moment (EDM),[2]

$$\begin{aligned}\mathcal{L}_{g-2} &= -\frac{eQ}{4m_l}\Delta a_l \bar{l}\sigma_{\mu\nu} l F^{\mu\nu}, \\ \mathcal{L}_{\text{EDM}} &= -\frac{i}{2} d_l \bar{l}\sigma_{\mu\nu}\gamma_5 l F^{\mu\nu},\end{aligned} \tag{13}$$

to the generic expressions in Eq. (8), the anomalous magnetic moment and EDM of lepton l can be readily read off as

$$\Delta a_l = -\frac{4m_l}{eQ_l}\,\text{Re}(A_{RL}), \qquad d_l = 2\,\text{Im}(A_{RL}), \tag{14}$$

respectively. The $\bar{l}' \to \bar{l}\gamma$ and $\bar{l}' \to \bar{l}\,\bar{l}\,l$ decay rates are given by

$$\Gamma(\bar{l}' \to \bar{l}\gamma) = \frac{(m^2_{l'} - m^2_l)^3}{4\pi m^3_{l'}}(|A_{L'R}|^2 + |A_{R'L}|^2) \tag{15}$$

and [6]

$$\begin{aligned}\Gamma(\bar{l}' \to \bar{l}\,\bar{l}\,l) =& \frac{m^5_{l'}}{3(8\pi)^3}\left[\frac{|g_{R'LRL}|^2}{8} + |g_{R'RLL}|^2\right. \\ &+ 32\left|\frac{eA_{R'L}}{m_{l'}}\right|^2 \log\left(\frac{m^2_{l'}}{m^2_l} - \frac{11}{4}\right) \\ &\left. + 16\text{Re}\left(\frac{eA_{R'L}g^*_{L'LLL}}{m_{l'}}\right) + 8\text{Re}\left(\frac{eA_{R'L}g^*_{L'LRR}}{m_{l'}}\right)\right] \\ &+ L \leftrightarrow R,\end{aligned} \tag{16}$$

respectively. While the $l'N \to lN$ conversion rate ratio is governed by

$$\mathcal{B}_{l'N\to eN} = \frac{\omega_{\text{conv}}}{\omega_{\text{capt}}}, \tag{17}$$

with

$$\begin{aligned}\omega_{\text{conv}} =& \left|\frac{A^*_{R'L}D}{2m_{l'}} + 2[2g^*_{LV}(u) + g^*_{LV}(d)]V^{(p)}\right. \\ &\left. + 2[g^*_{LV}(u) + 2g^*_{LV}(d)]V^{(n)}\right|^2 + L \leftrightarrow R.\end{aligned} \tag{18}$$

The numerical values of D, V, and ω_{capt} are taken from Refs. [10,11] and are collected in Appendix B.

C. Z-penguin amplitudes

The calculation of the Z-penguin amplitude is quite complicated and subtle. Some explanations are needed.

The interaction involving a Z boson is given by

$$\begin{aligned}\mathcal{L}^Z_{\text{int}} =& -\bar{l}\not{Z}(g^Z_{l_L}P_L + g^Z_{l_R}P_R)l - \bar{\psi}_{Lp}\not{Z}g^Z_{\psi_{Lp}}\psi_{Lp} \\ &- \bar{\psi}_{Rq}\not{Z}g^Z_{\psi_{Rq}}\psi_{Rq} - ig^Z_{\phi_{La}}(\phi^*_{La}\partial^\mu\phi_{La} - \partial^\mu\phi^*_{La}\phi_{La}) \\ &- ig^Z_{\phi_{Ra}}(\phi^*_{Ra}\partial^\mu\phi_{Ra} - \partial^\mu\phi^*_{Ra}\phi_{Ra}) + \ldots,\end{aligned} \tag{19}$$

with

$$g^Z_X = \frac{e}{\sin\theta_W\cos\theta_W}(T_3 - \sin^2\theta_W Q)_X, \tag{20}$$

for $X = l_{L(R)}$, $\psi_{L(R)p}$ and $\phi_{L(R)a}$ in the weak eigenstates. Since $\mathcal{L}_{\text{int}}$ transforms as a singlet under the SM gauge group, the g^Z_X of various fields are related through

$$g^Z_{l_{L(R)}} - g^Z_{\psi_{R(L)p}} - g^Z_{\phi a} = 0, \tag{21}$$

if the corresponding coupling $g^{lpa}_{lL(R)}$ in Eq. (4) is nonvanishing.

Although the couplings $g^Z_{\psi_{L(R)},\phi_{L(R)}}$ are diagonal in the weak bases, it may have off-diagonal terms in the mass bases. In the mass bases, the interacting Lagrangian involving a Z boson is given by

$$\begin{aligned}\mathcal{L}^Z_{\text{int}} =& -\bar{l}\not{Z}(g^Z_{l_L}P_L + g^Z_{l_R}P_R)l - \bar{\psi}_m\not{Z} \\ &\times (g^Z_{\psi_L mn}P_L + g^Z_{\psi_R mn}P_R)\psi_n \\ &- ig^Z_{\phi ij}(\phi^*_i\partial^\mu\phi_j - \partial^\mu\phi^*_i\phi_j) + \ldots,\end{aligned} \tag{22}$$

with

$$\begin{aligned} g^Z_{\phi ij} &= U^L_{ia}g^Z_{\phi_{La}}U^{\dagger L}_{aj} + U^R_{ia}g^Z_{\phi_{Ra}}U^{\dagger R}_{aj}, \\ g^Z_{\psi_{L(R)}mn} &= V^{L(R)}_{mp}g^Z_{\psi_{L(R)p}}V^{\dagger L(R)}_{pn}. \end{aligned} \tag{23}$$

[2]We use the convention where $D_\mu = \partial_\mu + ieQA_\mu$ with $e = +|e|$.

The one-loop amplitude for $l \to l'Z$ consists of two diagrams shown in Fig. 1 and two additional diagrams involving self-energy diagrams with Z attached to external lines. The resulting amplitude is given by (neglecting m_l, $m_{l'}$ and q^2)

$$\begin{aligned} iM = {} & \frac{i}{16\pi^2}\bar{u}'(g^{mi*}_{l'L}P_R + g^{mi*}_{l'R}P_L)\not{\epsilon}^*[(g^Z_{l_L}\delta_{ij}\delta_{mn} - g^Z_{\psi_R mn}\delta_{ij} - g^Z_{\phi ij}\delta_{mn})P_L + (g^Z_{l_R}\delta_{ij}\delta_{mn} - g^Z_{\psi_L mn}\delta_{ij} - g^Z_{\phi ij}\delta_{mn})P_R] \\ & \times (g^{nj}_{lL}P_L + g^{nj}_{lR}P_R)u\left[\frac{1}{2}\left(\frac{2}{4-d} - \gamma_E + \ln\frac{4\pi}{M^2}\right) - F_Z(m^2_{\psi_m}, m^2_{\psi_n}, m^2_{\phi_i}, m^2_{\phi_j}, M^2)\right] \\ & + \frac{i}{16\pi^2}(g^Z_{\psi_R mn} - g^Z_{\psi_L mn})\bar{u}'(g^{mi*}_{l'L}P_R + g^{mi*}_{l'R}P_L)\not{\epsilon}^*(g^{ni}_{lL}P_L - g^{ni}_{lR}P_R)uG_Z(m^2_{\psi_m}, m^2_{\psi_n}, m^2_{\phi_i}), \end{aligned} \tag{24}$$

where d is the number of the space-time dimension, γ_E is the Eular number and F_Z and G_Z are the loop functions whose explicit forms are shown in Appendix B. Note that M is an arbitrary mass parameter introduced to balance dimension. We will return to it later.

Note that the divergent part contained in the first term is indeed vanishing by requiring the $l - \psi - \phi$ interaction $\mathcal{L}_{\rm int}$ in Eq. (4) be invariant under the SM gauge group, i.e., we have

$$\begin{aligned} & g^{mi*}_{l'L(R)}(g^Z_{l_{L(R)}}\delta_{ij}\delta_{mn} - g^Z_{\psi_{R(L)}mn}\delta_{ij} - g^Z_{\phi ij}\delta_{mn})g^{nj}_{lL(R)} \\ & \quad = g^{lpa*}_{l'L(R)}(g^Z_{l_{L(R)}} - g^Z_{\psi_{R(L)}p} - g^Z_{\phi a})g^{lpa}_{lL(R)} = 0, \end{aligned} \tag{25}$$

where sum over indices are understood and Eq. (21) has been used in the last step. The nondivergent part, namely the one with F_Z, survives. Note that by the same token the dependence on the arbitrary mass parameter M cancels. The resulting Wilson coefficients will be given later. It is easy to see that in the non-mixing case ($U = V = \mathbf{1}$), the whole first term (including the F_Z term) is vanishing.

As a cross check, we note that the same expression of iM can be use to obtain the lowest order γ-penguin amplitude by replacing each g^Z by the corresponding eQ. Since under these replacement $(g^Z_{l_{L(R)}}\delta_{ij}\delta_{mn} - g^Z_{\psi_{R(L)}mn}\delta_{ij} - g^Z_{\phi ij}\delta_{mn}) \to e(Q_l - Q_\psi - Q_\phi)\delta_{ij}\delta_{mn} = 0$ and $(g^Z_{\psi_L mn} - g^Z_{\psi_R mn}) \to e(Q_\psi - Q_\psi)\delta_{mn} = 0$, the corresponding $\bar{u}'\not{\epsilon}^* u$ term is vanishing as expected.

D. Wilson coefficients

Induced by the interaction given in Eq. (3) the Wilson coefficients for the effective Lagrangian in Sec. II A are calculated to be

$$\begin{aligned} A_{M'N} = {} & \frac{e}{32\pi^2}[(m_l g^{ni*}_{l'M}g^{ni}_{lM} + m_{l'}g^{ni*}_{l'N}g^{ni}_{lN}) \\ & \times (Q_{\phi_i}F_1(m^2_{\psi_n}, m^2_{\phi_i}) - Q_{\psi_n}F_1(m^2_{\phi_i}, m^2_{\psi_n})) \\ & + m_{\psi_n}g^{ni*}_{l'M}g^{ni}_{lN}(Q_{\phi_i}F_3(m^2_{\psi_n}, m^2_{\phi_i}) \\ & - Q_{\psi_n}F_2(m^2_{\phi_i}, m^2_{\psi_n}))], \end{aligned} \tag{26}$$

for $M \neq N$, but with M, $N = L$, R, and F_i are loop functions collected in Appendix B. The Wilson coefficients in Eq. (12) are

$$\begin{aligned} g^P_{R'R} = {} & \frac{1}{16\pi^2}\{g^{ni*}_{l'R}g^{ni}_{lR}[Q_{\psi_n}G_2(m^2_{\phi_i}, m^2_{\psi_n}) + Q_{\phi_i}G_1(m^2_{\psi_n}, m^2_{\phi_i})] + m_{\psi_n}(m_l g^{ni*}_{l'R}g^{ni}_{lL} + m_{l'}g^{ni*}_{l'L}g^{ni}_{lR})[Q_{\psi_n}G_3(m^2_{\phi_i}, m^2_{\psi_n}) \\ & + Q_{\phi_i}G_3(m^2_{\psi_n}, m^2_{\phi_i})]\}, \\ g^Z_{R'R} = {} & -\frac{1}{16\pi^2 m_Z^2 \sin 2\theta_W}2\kappa_{Rijmn}g^{mi*}_{l'R}g^{nj}_{lR}F_Z(m^2_{\psi_m}, m^2_{\psi_n}, m^2_{\phi_i}, m^2_{\phi_j}, m^2_Z) \\ & - \frac{e}{16\pi^2 m_Z^2 \sin 2\theta_W}2\Delta T_{3\psi mn}g^{mi*}_{l'R}g^{ni}_{lR}G_Z(m^2_{\psi_m}, m^2_{\psi_n}, m^2_{\phi_i}), \\ g^Z_{L'L} = {} & -\frac{1}{16\pi^2 m_Z^2 \sin 2\theta_W}2\kappa_{Lijmn}g^{mi*}_{l'L}g^{nj}_{lL}F_Z(m^2_{\psi_m}, m^2_{\psi_n}, m^2_{\phi_i}, m^2_{\phi_j}, m^2_Z) \\ & + \frac{e}{16\pi^2 m_Z^2 \sin 2\theta_W}2\Delta T_{3\psi mn}g^{mi*}_{l'L}g^{ni}_{lL}G_Z(m^2_{\psi_m}, m^2_{\psi_n}, m^2_{\phi_i}), \\ g^B_{R'LRL} = {} & \frac{1}{16\pi^2}F(m^2_{\psi_m}, m^2_{\psi_n}, m^2_{\phi_i}, m^2_{\phi_j})(g^{mi^*}_{l'R}g^{mj}_{lL}g^{nj*}_{lR}g^{ni}_{lL} - 2\eta g^{mi^*}_{l'R}g^{mj*}_{lR}g^{ni}_{lL}g^{nj}_{lL}), \\ g^B_{R'RRR} = {} & \frac{1}{16\pi^2}\left[\frac{\eta}{2}g^{mi*}_{l'R}g^{mj*}_{lR}g^{ni}_{lR}g^{nj}_{lR}F(m^2_{\psi_m}, m^2_{\psi_n}, m^2_{\phi_i}, m^2_{\phi_j}) - \frac{1}{4}g^{mi*}_{l'R}g^{mj}_{lR}g^{nj*}_{lR}g^{ni}_{lR}G(m^2_{\psi_m}, m^2_{\psi_n}, m^2_{\phi_i}, m^2_{\phi_j})\right], \\ g^B_{R'RLL} = {} & \frac{1}{16\pi^2}\left\{-\frac{1}{4}G(m^2_{\psi_m}, m^2_{\psi_n}, m^2_{\phi_i}, m^2_{\phi_j})(g^{mi^*}_{l'R}g^{mj}_{lR}g^{nj*}_{lL}g^{ni}_{lL} + \eta g^{mi^*}_{l'R}g^{mj}_{lL}g^{ni}_{lL}g^{nj}_{lR}) - \frac{1}{2}g^{mi*}_{l'R}g^{mj}_{lL}g^{nj*}_{lL}g^{ni}_{lR}F(m^2_{\psi_m}, m^2_{\psi_n}, m^2_{\phi_i}, m^2_{\phi_j}) \right. \\ & \left. + \frac{\eta}{4}g^{mi*}_{l'R}g^{mj*}_{lL}g^{ni}_{lR}g^{nj}_{lL}G(m^2_{\psi_m}, m^2_{\psi_n}, m^2_{\phi_i}, m^2_{\phi_j})\right\}, \end{aligned} \tag{27}$$

with

$$\kappa_{L(R)ijmn} \equiv \sin 2\theta_W (g^Z_{l_{L(R)}} \delta_{ij}\delta_{mn} - g^Z_{\psi_{R(L)}mn}\delta_{ij} - g^Z_{\phi ij}\delta_{mn})/e,$$
$$\Delta T_{3\psi mn} \equiv V^R_{mp} T_{3\psi_{Rp}} V^{\dagger L}_{pn} - V^L_{mp} T_{3\psi_{Lp}} V^{\dagger R}_{pn}, \quad (28)$$

loop functions F and $G_{(i)}$ shown in Appendix B and $\eta = 1(0)$ for Majorana (Dirac) fermionic ψ. Other g can be obtained from the above ones by exchanging R and L. Note that for definiteness we take $M = m_Z$ in F_Z. As before, the summation on m, n, i, j is understood.

E. Two cases

We consider two complementary cases.

1. Case I

In the first case, namely case I, there is no built-in cancellation mechanism. The amplitudes may contain N different subamplitudes, each of which comes from one of the loop diagrams as shown in Fig. 1,

$$A = \sum_{j=1}^{N} A_j. \quad (29)$$

We will constrain parameters from data by switching on various diagrams (subamplitudes) one at a time. The corresponding Wilson coefficients of a typical subamplitude can be obtained by using formulas in Sec. II D, but with the replacement,

$$g^{ni}_{lM} \to g_{lM}, \quad (30)$$

with all summation on n and l suspended. Since there is no built-in cancellation in this case, different subamplitudes are, in principle, independent from each other. Although it is likely to have various amplitudes appear at the same time in a realistic model calculation and interfere with each other, the interference effects only become important if the amplitudes are of similar size. Hence, our analysis is not only valid when the sizes are different (hence, constraining the most dominant amplitude) but also can provide information on regions where interference may be important.

2. Case II

In case II, there is a built-in cancellation such as a GIM or a super-GIM mechanism in the NP sector. This case is complementary to the previous one. Some of the subamplitudes in Eq. (29) are intimately related. We have to group them to allow the cancellation mechanism to do its job first. The grouped amplitudes should be viewed as new sub-amplitudes and we will turn them on one at a time to constrain their sizes from data. To be specify, we consider

$$g^{ni}_{lM} \to g^i_{lM} = g_{lM}\Gamma^{il}_M, \quad (31)$$

where we have $M = L, R$ and g_{lM} is real as the phase is absorbed into Γ. Note that the matrix Γ is similar and related to the mixing matrix U, but is not identical to it. These Γ satisfy the following relations:

$$\Gamma^{\dagger li}_M m_i^2 \Gamma^{il'}_N = (m^2_\phi)^{ll'}_{MN}, \qquad \Gamma^{\dagger li}_M \Gamma^{il'}_N = \delta^{ll'}\delta_{MN}. \quad (32)$$

A typical expression of Wilson coefficients given in Sec. II D is transformed in the following way:

$$\sum_i g^{i*}_{\mu M} f(m^2_\psi, m^2_{\phi_i}) g^i_{eN} \to m^2_\phi \frac{\partial}{\partial m^2_\phi} f(m^2_\psi, m^2_\phi) g_{\mu M} g_{eN} \delta^{MN}_{\mu e}, \quad (33)$$

where m^2_ϕ is the average mass squared of ϕ_i, and the mixing angle $\delta^{MN}_{\mu e}$ is defined in the usual way to be [12]

$$\delta^{MN}_{\mu e} \equiv \frac{1}{m^2_\phi}\Gamma^{M\dagger}_{\mu i}(m^2_{\phi_i} - m^2_\phi)\Gamma^N_{ie} = \frac{(m^{2MN}_\phi)_{\mu e}}{m^2_\phi}. \quad (34)$$

The Wilson coefficients in this case can be obtained readily by applying the above replacements to the generic formulas collected in Sec. II D.

Note that in the Z-penguin amplitude, the zeroth and first-order terms in the $\kappa_{L(R)}F_Z$ part are vanishing. The leading order contribution is at the level of $\delta_{LR}\delta_{RL}$, which is beyond the accuracy of the present analysis and is neglected.

III. RESULTS

Numerical results in cases I and II are given in this section. Unless specified explicitly, experimental inputs are taken from Table I and Ref. [2].

A. Case I

In Fig. 2 we show the allowed parameter space for $Q_{\phi,\psi}|g_{\mu L(R)}|^2/m^2_\psi$ and $Q_{\phi,\psi}\mathrm{Re}(g^*_{\mu R}g_{\mu L})/m_\psi$ constrained by the measured Δa_μ with exclusion of $|g_{\mu L(R)}|^2$, $|g_{\mu L}g_{\mu R}| > 4\pi$ and $m_{\psi,\phi} < 100$ GeV.[3] The latter requirements are to ensure perturbativity and to satisfy the experimental bounds on the masses of exotic particles [2]. Bands denoted with ϕ or ψ are allowed regions obtained through contributions from diagrams with ϕ or ψ interacting with a photon [see Figs. 1(a) and 1(b)].

[3]It is easy to see that $|g_{\mu L(R)}|^2 > 4\pi$ and $m_\psi < 100$GeV implies $|g_{\mu L(R)}|^2/m^2_\psi > 4\pi/(100)^2$ GeV^{-2} and $|g_{\mu L}g_{\mu R}|^2/m_\psi > 4\pi/100$GeV^{-1}, while $|g_{\mu L(R)}|^2 > 4\pi$ and $m_\phi < 100$ GeV implies $|g_{\mu L(R)}|^2/m^2_\psi = (|g_{\mu L(R)}|^2/m^2_\phi) \times (m_\phi/m_\psi)^2 > 4\pi/(100)^2 \times (m_\phi/m_\psi)^2$ GeV^{-2} and $|g_{\mu L}g_{\mu R}|^2/m_\psi > (4\pi/100) \times (m_\phi/m_\psi)$ GeV^{-1}. These excluded regions are shown by shaded areas with horizontal or inclined boundaries.

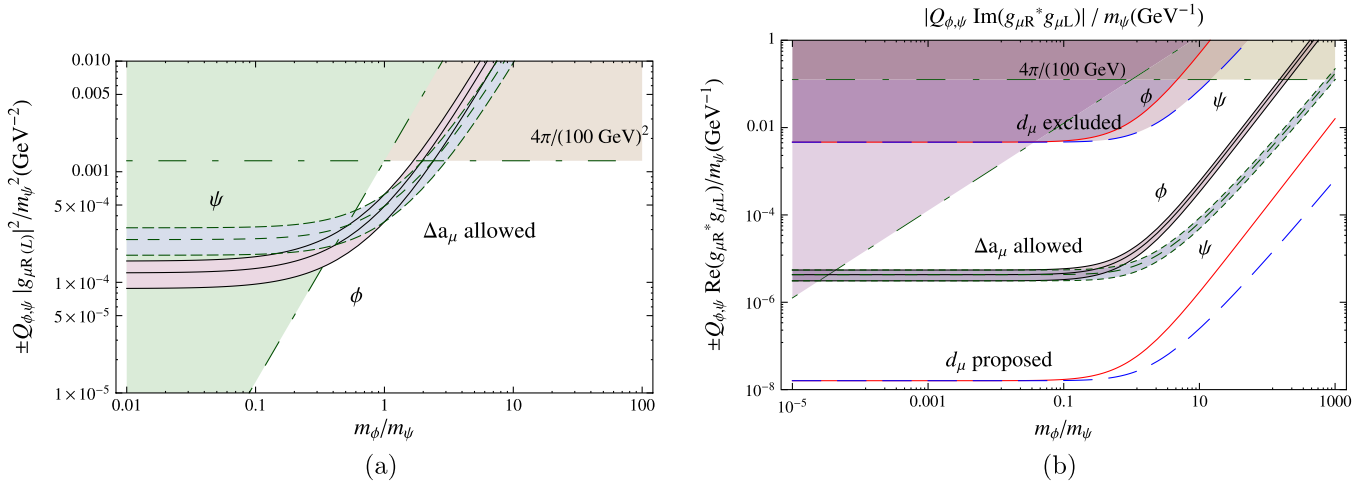

FIG. 2 (color online). (a) Allowed parameter space for $\pm Q_{\phi,\psi}|g_{\mu L(R)}|^2/m_\psi^2$ constrained by Δa_μ (bands with solid or dashed lines) with exclusion of $|g_{\mu L(R)}|^2 > 4\pi$ and $m_{\psi,\phi} < 100$ GeV (shaded regions with dot-dashed lines). (b) Allowed parameter space for $\pm Q_{\phi,\psi}\mathrm{Re}(g_{\mu R}^* g_{\mu L})/m_\psi$ constrained by Δa_μ with exclusion of $|g_{\mu L} g_{\mu R}| > 4\pi$ and $m_{\psi,\phi} > 100$ GeV. Excluded parameter space (shaded regions with solid or dashed lines) of $|Q_{\phi,\psi}\mathrm{Im}(g_{\mu R}^* g_{\mu L})|/m_\psi$ from the muon EDM bound and the expected sensitivity are also shown.

Excluded parameter space of $|Q_{\phi,\psi}\mathrm{Im}(g_{\mu R}^* g_{\mu L})|/m_\psi$ confronting the muon electric dipole moment (EDM) bound [2] is also shown in Fig. 2(b).

From Fig. 2(a), we see that the allowed regions on $Q_\phi|g_{\mu L(R)}|^2/m_\psi^2$ and $-Q_\psi|g_{\mu L(R)}|^2/m_\psi^2$ are similar and the signs of $Q_{\phi,\psi}$ are constrained by data. Note that the allowed parameter space is quite limited. Indeed, it is almost closed by the bounds from $|g_{\mu L(R)}|^2 < 4\pi$ and $m_\psi > 100$ GeV and $m_\phi > 100$ GeV. The allowed region is around $\pm Q_{\phi,\psi}|g_{\mu L(R)}|^2/m_\psi^2 \simeq 10^{-4} \sim 10^{-3}$ GeV^{-2} and $m_\phi/m_\psi \simeq 0.3 \sim 3$, which implies that for $m_{\phi,\psi}$ of a few hundred GeV, the couplings $Q_{\phi,\psi}|g_{\mu L(R)}|^2$ are required to be of order $\mathcal{O}(1) \sim \mathcal{O}(10)$, which are rather large, and are even larger for heavier $m_{\phi,\psi}$. To see it in another way, if we take the size of $g_{\mu L(R)}$ to be similar to that of the electric coupling e, we need $m_{\phi,\psi}$ to be as light as 10 to 30 GeV to reproduce the experimental result on Δa_μ. Thus, it is unlikely to use a chiral-type interaction ($g_{\mu L} \times g_{\mu R} = 0$) to generate the measured Δa_μ.

From Fig. 2(b), we see that the allowed parameter space is substantially larger. To reproduce the measured Δa_μ, the mass ratio has to be in the range of $\mathcal{O}(10^{-5}) \lesssim m_\phi/m_\psi \lesssim \mathcal{O}(10^{2,3})$, which is much wider than the one in Fig. 2(a). We note that the bands of the allowed parameter space behave rather differently in two regions roughly separated by $m_\phi/m_\psi = 0.1$. (i) For $m_\phi/m_\psi \lesssim 0.1$, the horizontal bands denoting the allowed parameter region for $\pm Q_{\phi,\psi}\mathrm{Re}(g_{\mu R}^* g_{\mu L})/m_\psi$ are around 4×10^{-6} GeV^{-1}. They are insensitive to m_ϕ/m_ψ, since the chiral enhancement factor m_ψ/m_μ compensates for the suppression from the heavy ψ mass. Note that m_ϕ/m_ψ can be as low as 3×10^{-5}, which implies that m_ψ up to 3×10^3 TeV is still capable of reproducing the measured Δa_μ in the extreme case, where we have a light ϕ [$m_\phi = \mathcal{O}(100)$ GeV] and large couplings [$|g_{\mu L} g_{\mu R}| = \mathcal{O}(4\pi)$]. (ii) For $m_\phi/m_\psi \gtrsim 0.1$, the allowed bands rise with the mass ratio. The muon $g-2$ is more sensitive to the diagram with ψ interacting with a photon [as depicted in Fig. 1(b)] than to the other diagram; hence, the constraint on $-Q_\psi\mathrm{Re}(g_{\mu R}^* g_{\mu L})/m_\psi$ is more severe than the one on $+Q_\phi\mathrm{Re}(g_{\mu R}^* g_{\mu L})/m_\psi$. Indeed, in the large m_ϕ/m_ψ region, the suppressions from a large ϕ mass should be larger in diagrams with ϕ interacting with a photon and, hence, require larger couplings to compensate for the effect. We see that the mass ratio m_ϕ/m_ψ can go up to 200 (1000) along the ϕ (ψ) band, which corresponds to allowing m_ϕ to be as large as 20 (100) TeV in the extreme situation.

As noted previously, in Fig. 2(b) we also show the excluded region of $|Q_{\phi,\psi}\mathrm{Im}(g_{\mu R}^* g_{\mu L})|/m_\psi$ from the muon EDM bound. We see that the bound is three orders of magnitude higher than that in the allowed $\pm Q_{\phi,\psi}\mathrm{Re}(g_{\mu R}^* g_{\mu L})/m_\psi$ bands. To constrain the former to the level of the latter, the EDM sensitivity needs to be improved. In fact, some proposed EDM searches (see, for example Ref. [13]) are aimed at a four to five orders of magnitude improvement on the sensitivity and may be able to probe the imaginary part of $g_{\mu R}^* g_{\mu L}$ better than its real part.

We now turn to μ LFV processes, including $\mu \to e\gamma$, $\mu \to 3e$, $\mu\mathrm{Ti} \to e\mathrm{Ti}$, and $\mu\mathrm{Au(Al)} \to e\mathrm{Au(Al)}$ transitions. In Figs. 3 and 4, we show the parameter space excluded by various bounds and the one corresponding to projections from the expected sensitivities on these μ LFV processes, through contributions from photonic and

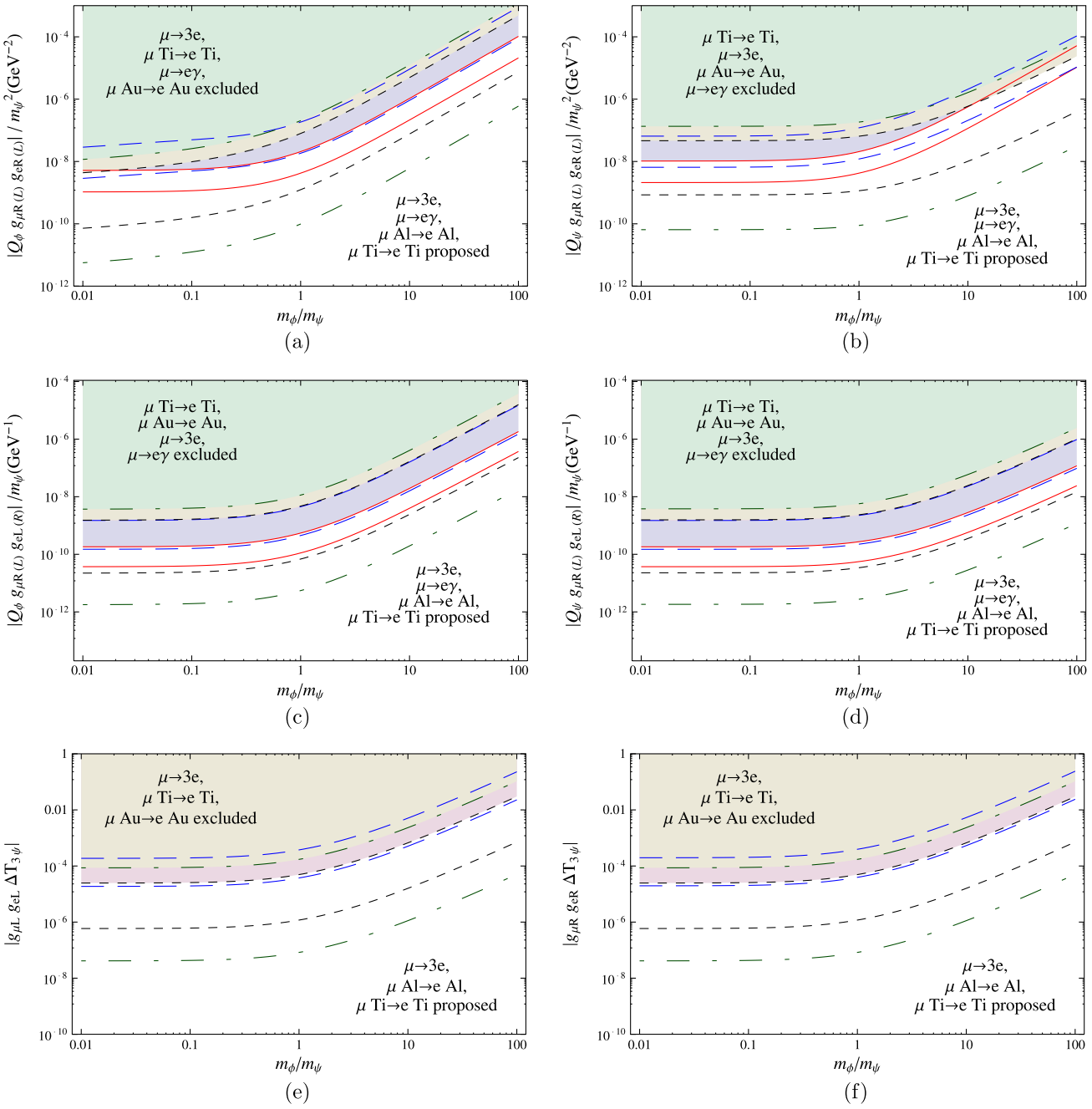

FIG. 3 (color online). (a)-(d): Parameter space excluded (projected) by various bounds (expecting sensitivities) on μ LFV processes through contributions from photonic penguins. Note that solid, dashed, dot-dashed, and short-dashed lines denote results from $\mu \to e\gamma$, $\mu \to 3e$, $\mu\mathrm{Ti} \to e\mathrm{Ti}$, and $\mu\mathrm{Au(Al)} \to e\mathrm{Au(Al)}$ processes, respectively. (e) and (f): Same as (a)-(d), but through contributions from Z penguins.

Z-penguin diagrams. To be specific, for the proposed sensitivities, the conservative values of the future sensitivities quoted in Table I are used. Note that the photonic penguins contribute to $\mu \to 3e$ and $\mu N \to eN$ through the so-called F_2 penguin, which is similar to those contributing to Δa_μ and $\mu \to e\gamma$, and the F_1 penguin, while the Z penguins only contribute to $\mu \to 3e$ and $\mu N \to eN$ decays. Note that the Z-penguin amplitudes contribute through the $|g_{\mu R(L)} g_{eR(L)} \Delta T_{3\psi}|$ and $|g_{\mu R(L)} g_{eR(L)} \kappa_{R(L)}|$ parts. The former contribution is a function of the mass ratio m_ϕ/m_ψ, while the latter one depends on both ϕ and ψ masses. The resulting constraints are plotted in Figs. 3(e), 3(f), and 4. It should be noted that Figs. 3 and 4 can still be useful if the experimental bounds change. For example, if a bound is reduced by a factor of k, the new plot can be easily updated by reducing the present plot by a factor of $\sqrt{k}$.

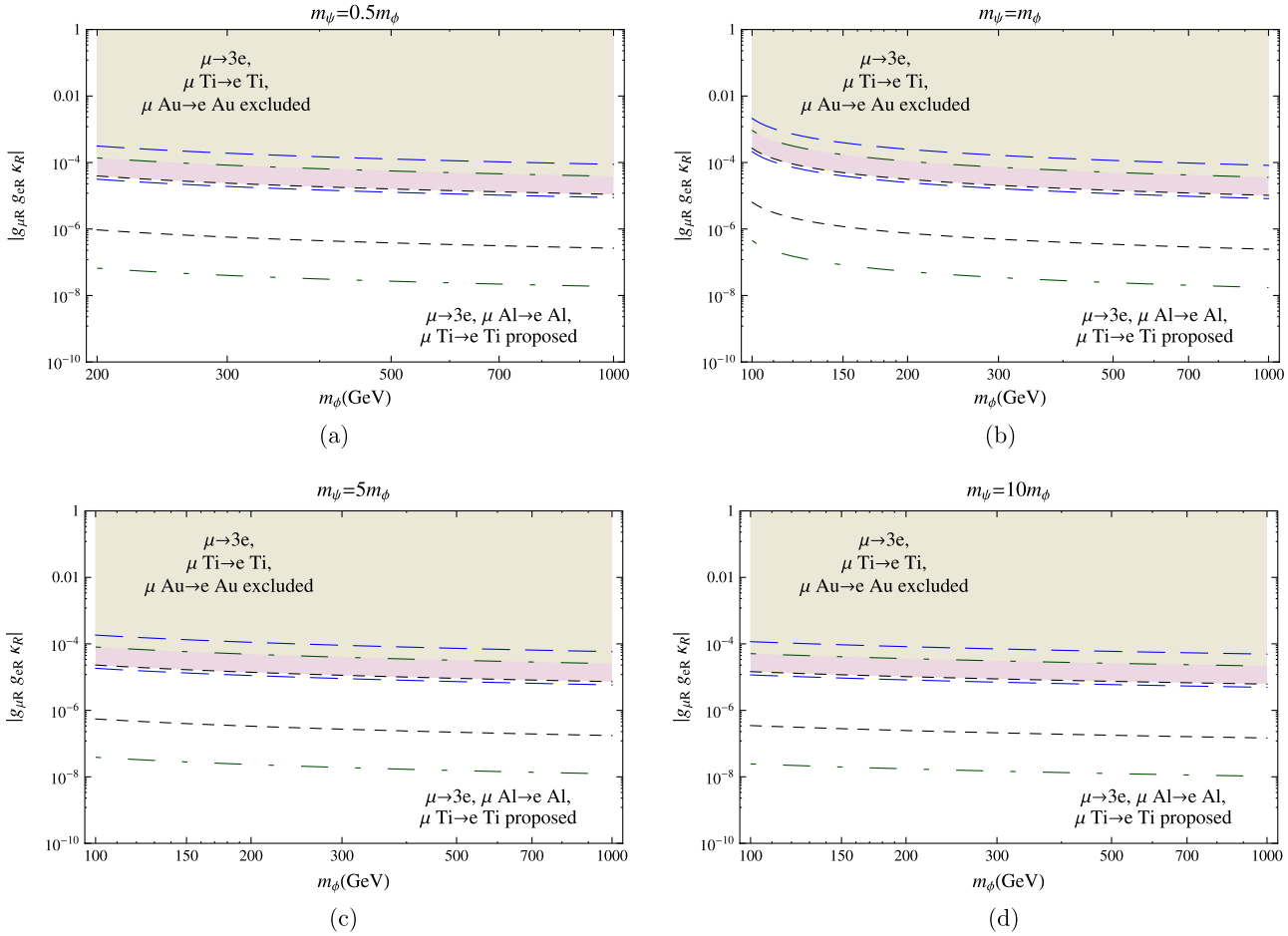

FIG. 4 (color online). (a)-(d): Parameter space excluded (projected) by various bounds (expecting sensitivities) on μ LFV processes through contributions from Z penguins with different choices of mass ratios. Note that dashed, dot-dashed, and short-dashed lines denote results from $\mu \to 3e$, $\mu\mathrm{Ti} \to e\mathrm{Ti}$, and $\mu\mathrm{Au(Al)} \to e\mathrm{Au(Al)}$ processes, respectively. Note that these plots also apply to the $R \leftrightarrow L$ cases.

Note that the combinations of couplings $|Q_{\phi,\psi} g_{\mu R(L)} g_{eR(L)}|$, $|Q_{\phi,\psi} g_{\mu R(L)} g_{eL(R)}|$ (from photonic penguin) and $|g_{\mu R(L)} g_{eR(L)} \Delta T_{3\psi}|$, $|g_{\mu R(L)} g_{eR(L)} \kappa_{L(R)}|$ (from Z penguin) have different sensitivities on the experimental constraints, and the sensitivities change with $m_{\psi,\phi}$. For heavier $m_{\phi,\psi}$, the contributions from the photonic penguins decrease and the Z-penguin contributions, where the nondecoupling effect is working, dominate. By comparing Figs. 3(a) and 3(b) to Figs. 3(e), 3(f), and 4,[4] we find that (i) in the range of $m_\psi \lesssim \mathcal{O}(100)$ GeV the photonic penguin contributions dominate over the Z-penguin ones, (ii) in the range of the $\mathcal{O}(100)$ GeV $\lesssim m_\psi \lesssim \mathcal{O}(100)$ TeV, the photonic penguin contributions from the $Q_{\phi,\psi} g_{\mu R(L)} g_{eL(R)}$ terms dominate over the Z-penguin contributions, which are, however, still larger than the photonic penguin contributions from the $Q_{\phi,\psi} g_{\mu R(L)} g_{eR(L)}$ part, and for (iii) $m_\psi \gtrsim \mathcal{O}(100)$ TeV, the Z-penguin contributions dominate. The role that Z penguin plays is emphasized in Ref. [14].

Since NP contributions to Δa_μ and the $\mu^+ \to e^+\gamma$ decay are from similar diagrams, it will be useful to compare them. Using Figs. 2(b), 3(c), and 3(d), the present data on Δa_μ and $\mathcal{B}(\mu^+ \to e^+\gamma)$ lead to

$$\frac{g_{\mu R(L)} g_{eL(R)}}{g_{\mu R} g_{\mu L}} = \frac{g_{eL(R)}}{g_{\mu L(R)}} \leq 6.1 \times 10^{-5} \simeq \lambda^6, \qquad (35)$$

where we define $\lambda \equiv 0.2$. This ratio is much smaller than any known coupling ratio and mixing angle among the first and second generations. For example, the mass ratio $m_e/m_\mu \sim \lambda^{3\sim4}$, quark mixing in Cabibbo-Kobayashi-Maskawa matrix $V_{ud} = \sin\theta_c \sim \lambda$, and neutrino mixing $\sin\theta_{\nu 12} \sim \sqrt{\lambda}$ are all larger than the estimated $g_{eL(R)}/g_{\mu L(R)}$ coupling ratio. It seems that the present case is unnatural.

We see from Figs. 3(a)–3(d) that the present bound from $\mu \to e\gamma$ surpasses all other bounds. In particular, even the parameter space to be probed by the proposed $\mu \to 3e$ sensitivity is mostly excluded by the present $\mu \to e\gamma$ bound.

[4]Note that the plotted quantities in these figures have different powers of m_ψ.

This can be understood by using Fig. 5, where rate ratios of various modes through photonic penguins are given. We see that the ratios of LFV rates with respect to the $\mu \to e\gamma$ rate are all less than unity. Furthermore, we recall that the present experimental bounds on LFV rates are of similar orders of magnitude (see Table I). Therefore, the present bound on the $\mu \to e\gamma$ rate provides the most severe constraint.

Taking a closer look at Fig. 5, we see that, from Figs. 5(a) and 5(b), the $|Q_{\phi,\psi} g_{\mu R(L)} g_{eR(L)}|$ terms give $\mathcal{B}(\mu \to e\gamma) > \mathcal{B}(\mu N \to eN) \gtrsim \mathcal{B}(\mu \to 3e)$ and, from Figs. 5(c) and 5(d), the $|Q_{\phi,\psi} g_{\mu R(L)} g_{eL(R)}|$ terms give $\mathcal{B}(\mu \to 3e)/\mathcal{B}(\mu \to e\gamma) \simeq 0.006$, $\mathcal{B}(\mu\mathrm{Ti} \to e\mathrm{Ti})/\mathcal{B}(\mu \to e\gamma) \simeq 0.004$ and $\mathcal{B}(\mu\mathrm{Al} \to e\mathrm{Al})/\mathcal{B}(\mu \to e\gamma) \simeq 0.003$, where the first ratio is consistent with Ref. [6]. Hence, for $g_{\mu R(L)} g_{eL(R)}$ dominating models, the latest MEG bound implies

$$\mathcal{B}(\mu^+ \to e^+ e^+ e^-) \simeq 0.006 \times \mathcal{B}(\mu^+ \to e^+ \gamma) \lesssim 1.4 \times 10^{-14},$$
$$\mathcal{B}(\mu N \to eN) \simeq \mathcal{O}(10^{-3}) \times \mathcal{B}(\mu^+ \to e^+ \gamma) \lesssim \mathcal{O}(10^{-15}), \tag{36}$$

for $N =$ Au, Al and Ti. The above expecting limits are about two to three orders of magnitudes below the present experimental sensitivities (see Table I) and make the searches on LFV in the muon sector challenging in this case.

As noted in Sec. II A, it is possible to have box diagrams with the electron line in Figs. 1(c) and 1(d) replaced by a quark one and contribute to $\mu N \to eN$ conversions in some cases. The correlation to the $\mu \to 3e$ rate will be modified. We will discuss more on this situation in the discussion section.

Note that Z penguins give different rate ratios (not shown in Fig. 5), with $\mathcal{B}(\mu\mathrm{Al} \to e\mathrm{Al})/\mathcal{B}(\mu \to 3e) \simeq 10$, $\mathcal{B}(\mu\mathrm{Ti} \to e\mathrm{Ti})/\mathcal{B}(\mu \to 3e) \simeq 20$, and $\mathcal{B}(\mu\mathrm{Au} \to e\mathrm{Au})/\mathcal{B}(\mu \to 3e) \simeq 40$ roughly independent of the masses $m_{\phi,\psi}$. This pattern is different from the photonic penguin case as shown in Fig. 5. These rate ratios will be useful for identifying the underlying NP contributions.

In Fig. 6, we show the constraints on parameters that contribute through box diagrams, as depicted in Figs. 1(c) and 1(d), to the $\mu^+ \to 3e$ process. Both Dirac and Majorana cases are shown. We see in Fig. 6(a) that there is cancellation in the Majorana case and the sensitivity on the parameters is relaxed.

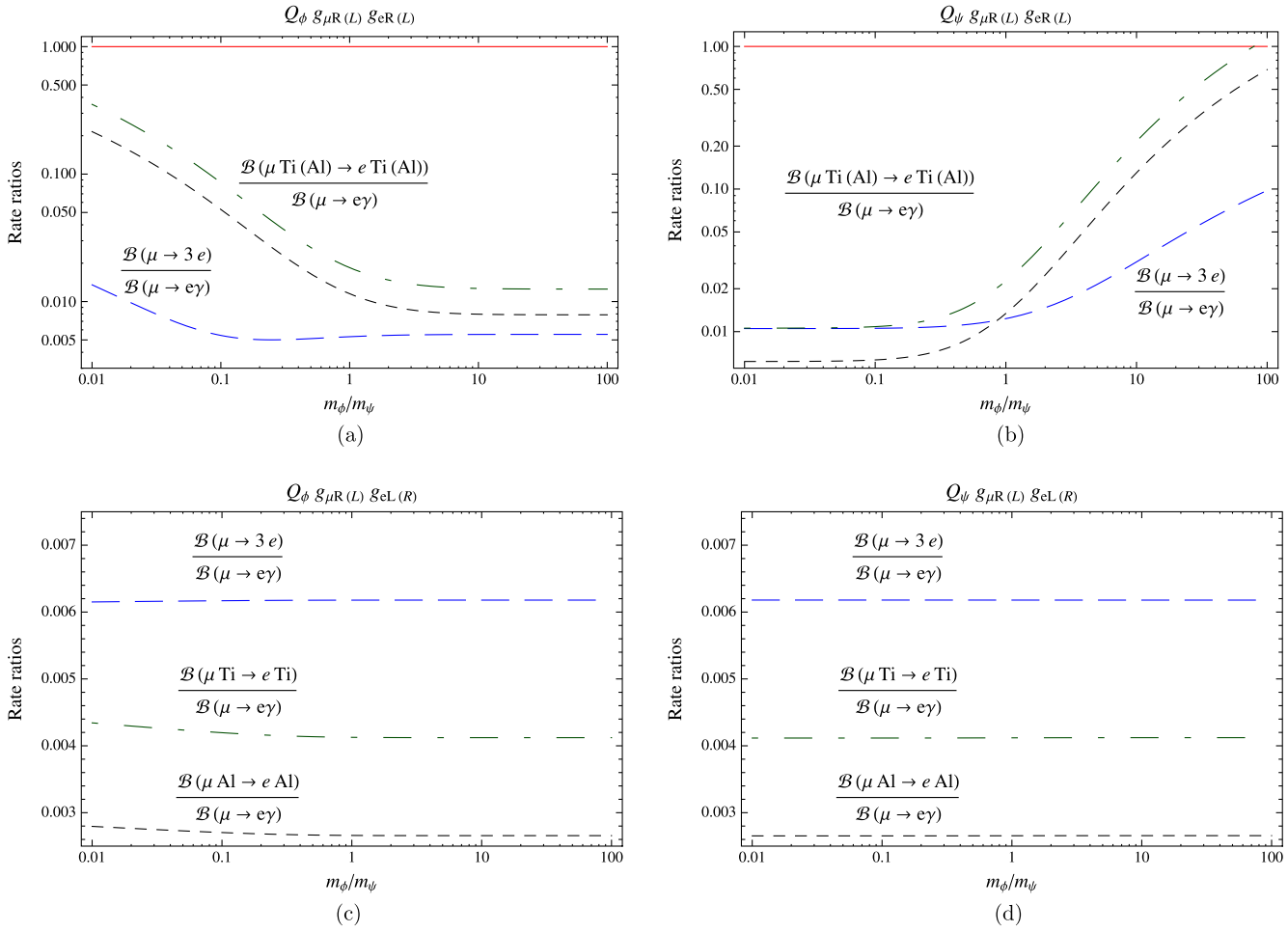

FIG. 5 (color online). Ratios of rates contributed from photonic penguins.

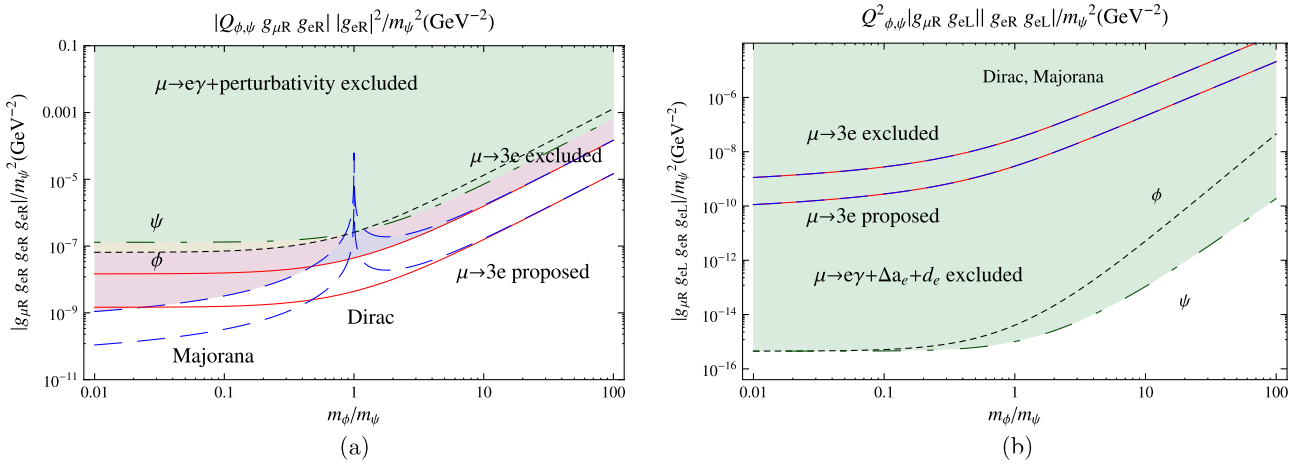

FIG. 6 (color online). Constraints on parameters that contribute through box diagrams to the $\mu^+ \to 3e$ process. Solid lines denote the $\mu \to 3e$ constraint or expectation in the Dirac case, while the dashed lines denote the Majorana case. Note that these plots also apply to the $R \leftrightarrow L$ cases.

Note that constraints on the same combinations of parameters can be obtained from penguin processes, including $\mu \to e\gamma$, Δa_e, EDM, and the perturbative bounds, as well. They are also shown in Fig. 6. We see that these constraints are usually much stronger than the ones from the box diagrams, except for $|g_{\mu R(L)} g_{eR(L)} g_{eR(L)} g_{eR(L)}|/m_\psi^2$ in the low m_ϕ/m_ψ region. In particular, the $\mu \to e\gamma$, Δa_e and the electron EDM constrain $(Q_{\phi,\psi}|g_{\mu R(L)} g_{eL(R)}|/m_\psi)(Q_{\phi,\psi} g_{eR(L)} g_{eL(R)}|/m_\psi)$ much deeper than $|g_{\mu R(L)} g_{eR(L)} g_{eL(R)} g_{eL(R)}|/m_\psi^2$ from the box diagrams. Hence, in general, these box diagrams do not play a major role in the $\mu^+ \to 3e$ decay.

B. Case II

We now turn to case II. In Fig. 7, the allowed regions for $\mp Q_{\phi,\psi} g_{\mu R} g_{\mu L} \mathrm{Re}(\delta_{RL})_{\mu\mu}/m_\psi$ constrained by the measured Δa_μ, with exclusions of $|g_{\mu L} g_{\mu R} \delta_{RL}| > 4\pi$ and $m_{\psi,\phi} < 100$ GeV, are shown. Excluded and projected parameter space of $|Q_{\phi,\psi} g_{\mu R} g_{\mu L} \mathrm{Im}(\delta_{RL})_{\mu\mu}|/m_\psi$ from the muon EDM bound and the expected sensitivity are also given on the same plot. For the plots of the allowed regions for $\pm Q_{\phi,\psi}|g_{\mu L(R)}|^2/m_\psi^2$, one is referred to Fig. 2(a), as they are common in both cases.

Comparing Fig. 7 to Fig. 2(b), we see that the allowed parameters in the upper m_ϕ/m_ψ region are similar. In contrast, they are relaxed substantially in the lower m_ϕ/m_ψ region in the present case. To reproduce the measured Δa_μ, we need to have $\mathcal{O}(10^{-2}) \lesssim m_\phi/m_\psi \lesssim \mathcal{O}(10^{2,3})$, where the minimum of the mass ratio is much higher than the one in the previous case. Recall that in case I, for $m_\phi/m_\psi \lesssim 0.1$, the allowed parameter region for $\pm Q_{\phi,\psi} \mathrm{Re}(g^*_{\mu R} g_{\mu L})/m_\psi$ are horizontal bands around 4×10^{-6} GeV^{-1} and m_ϕ/m_ψ can be as low as $\mathcal{O}(10^{-5})$. From Fig. 7, we see that as we move downward along the m_ϕ/m_ψ axis, the bands for the allowed regions for $\mp Q_{\phi,\psi} g_{\mu R} g_{\mu L} \mathrm{Re}(\delta_{RL})_{\mu\mu}/m_\psi$ bend upward in the low mass ratio region ($m_\phi/m_\psi < 1$) and the above parameters can be as large as 10^{-3} GeV^{-1}, which is three orders of magnitude higher than those in case I. We also note that the mass ratio m_ϕ/m_ψ cannot be smaller than 10^{-2} as the bands quickly run into the shaded regions, which correspond to the excluded $m_\phi < 100$ GeV and $|g_{\mu R} g_{\mu L} \mathrm{Re}(\delta_{RL})_{\mu\mu}| > 4\pi$ regions. In the present case, the mass of ψ cannot be larger than a few tens of TeV, while in case I it can be as high as a few thousand TeV in the extreme situation. The built-in cancellation mechanism reduces the amplitudes effectively and a too heavy ψ is incapable to produce a large enough Δa_μ. The effect of the cancellation is important in the low m_ϕ/m_ψ region and, consequently, relaxes the constraints on parameters.

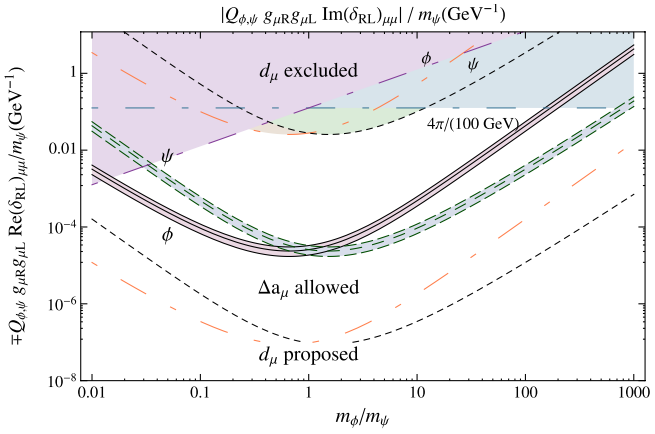

FIG. 7 (color online). Allowed parameter space for $\mp Q_{\phi,\psi} g_{\mu R} g_{\mu L} \mathrm{Re}(\delta_{RL})_{\mu\mu}/m_\psi$ constrained by Δa_μ with exclusion of $|g_{\mu L} g_{\mu R} \delta_{RL}| > 4\pi$ and $m_{\psi,\phi} > 100$ GeV. Excluded parameter space (shaded regions with solid or dashed lines) of $|Q_{\phi,\psi} g_{\mu R} g_{\mu L} \mathrm{Im}(\delta_{RL})_{\mu\mu}/m_\psi|$ from the muon EDM bound is also shown.

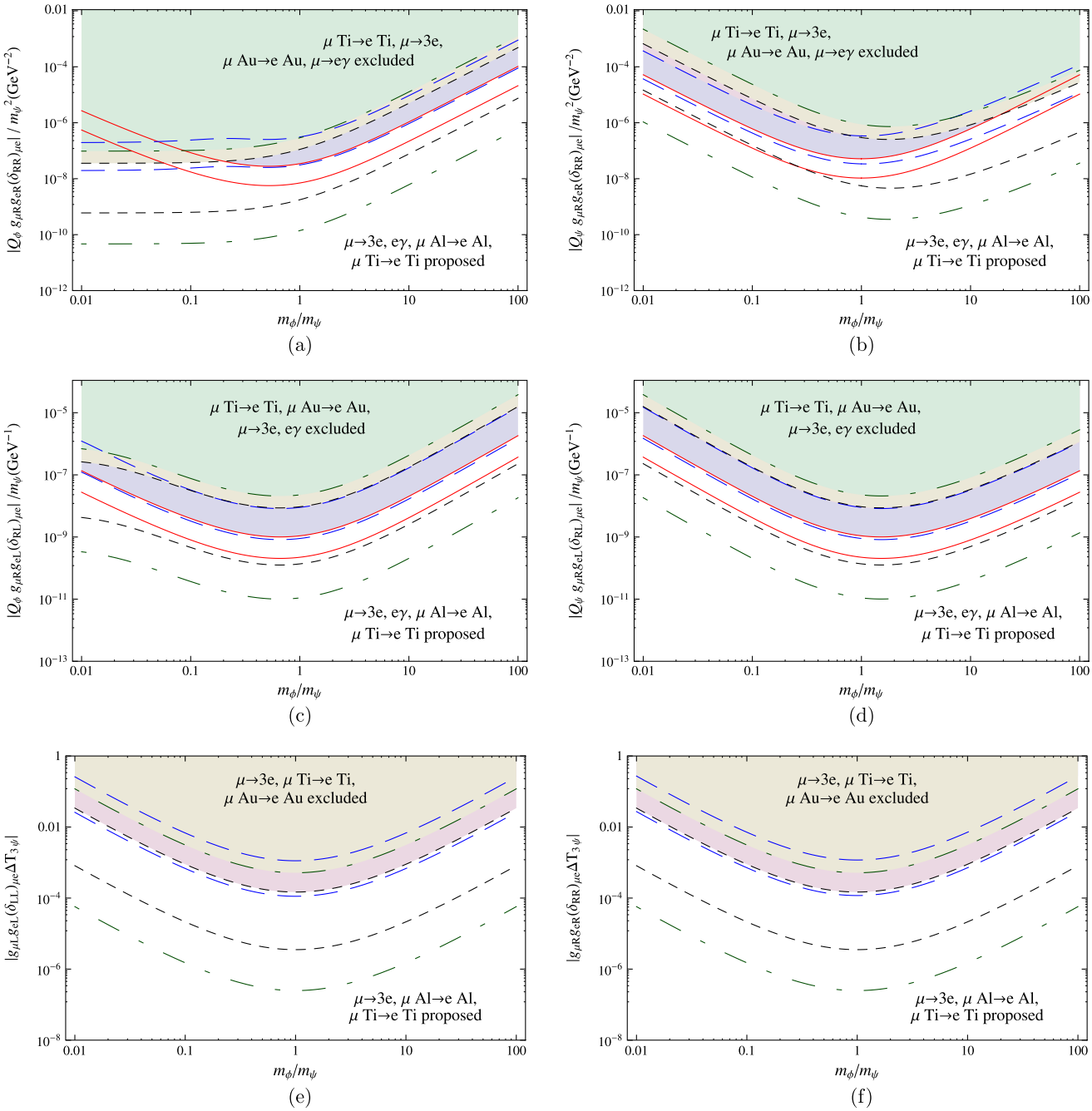

FIG. 8 (color online). Same as Fig. 3, but now in case II.

In fact, we expect to see the very feature in other penguin contributing channels as well.

In Fig. 8, we show the constrained and projected parameter space through penguin contributions by considering the experimental bounds and the proposed sensitivities.[5] We note that the photonic penguin contributions via the δ_{RL} term dominate over other contributions for m_ψ below $\mathcal{O}(10^3)$ TeV. For m_ψ beyond that, the Z-penguin contribution takes over. However, from the previous discussion on the muon anomalous magnetic moment, we see that to account for the measured Δa_μ, m_ψ cannot be heavier than a few tens of TeV. Hence, the Z-penguin contribution will be subdominant in this case.

By comparing the constraints from Δa_μ and $\mathcal{B}(\mu \to e\gamma)$ as shown in Figs. 7, 8(c), and 8(d), we obtain

$$\frac{g_{\mu R(L)} g_{eL(R)} \mathrm{Re}[(\delta_{RL(LR)})_{\mu e}]}{g_{\mu R} g_{\mu L} \mathrm{Re}[(\delta_{RL})_{\mu\mu}]} = \frac{g_{eL(R)}}{g_{\mu L(R)}} \frac{\mathrm{Re}[(\delta_{RL(LR)})_{\mu e}]}{\mathrm{Re}[(\delta_{RL})_{\mu\mu}]} \leq 4.2 \times 10^{-5} \simeq \lambda^6. \quad (37)$$

[5]For Z-penguin contributions, only those from $\Delta T_{3\psi}$ are shown, since the $\kappa_{L(R)}$ ones are highly suppressed.

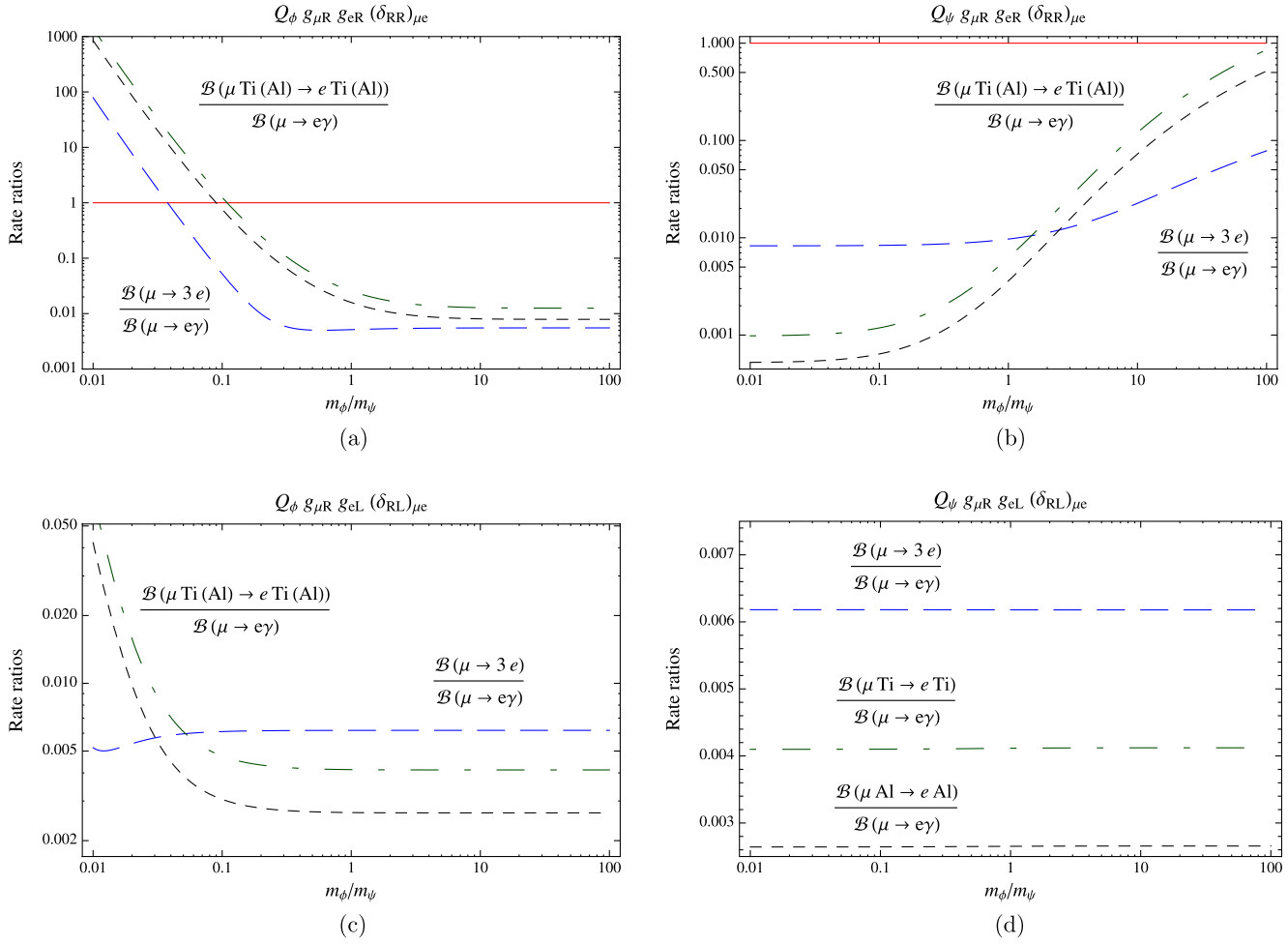

FIG. 9 (color online). Same as Fig. 5, but in case II.

If we estimate $g_{eL(R)}/g_{\mu L(R)}$ by using the lepton mass ratio $m_e/m_\mu \sim \lambda^{3\sim4}$, we see that a mixing angle ratio of $\mathrm{Re}[(\delta_{RL(LR)})_{\mu e}]/\mathrm{Re}[(\delta_{RL})_{\mu\mu}] \lesssim \lambda^{2\sim3}$, which is not unnatural, can easily satisfy the above bound. In this respect, case II is more reasonable and natural than case I, where the coupling ratio is highly hierarchical [see, Eq. (35)].

It is interesting to see from Fig. 8 that the $\mu \to e\gamma$ bound is not always the most stringent one. The bounds from $\mu \to 3e$ and $\mu N \to eN$ in Fig. 8(a) are almost the same as those in case I [see Fig. 3(a)], but the bound from $\mu \to e\gamma$ is relaxed up to more than two orders of magnitude in the low m_ϕ/m_ψ region and becomes less severe than other bounds. Similarly, comparing Fig. 8(c) with Fig. 3(c), we see that in the low m_ϕ/m_ψ region, both bounds from $\mu \to e\gamma$ and $\mu \to 3e$ are relaxed up to three orders of magnitude, while the changes on those from $\mu N \to eN$ are mild. We can infer that, similar to the Δa_μ case, the F_2 (photonic) penguin amplitudes exhibit cancellations in amplitudes in the low m_ϕ/m_ψ region and relax the constraints from $\mu \to e\gamma$ significantly, while the cancellations in the F_1 penguin contributions in $\mu \to 3e$ and $\mu N \to eN$ processes are mild. As a result, the bounds from $\mu N \to eN$ approach the $\mu \to e\gamma$ bound in this case, while in the previous case these two bounds are always apart.

The ratios of photonic-penguin contributing rates plotted in Fig. 9 show that $\mathcal{B}(\mu N \to eN)/\mathcal{B}(\mu \to e\gamma)$ and $\mathcal{B}(\mu \to 3e)/\mathcal{B}(\mu \to e\gamma)$ are enhanced compared with those in Fig. 5. In Fig. 9(a) we see that the ratios can be enhanced up to three orders of magnitude. In Fig. 9(c) the $\mathcal{B}(\mu N \to eN)/\mathcal{B}(\mu \to e\gamma)$ ratio is enhanced by one order of magnitude, while the $\mathcal{B}(\mu \to 3e)/\mathcal{B}(\mu \to e\gamma)$ ratio does not change much. It is very interesting that the rate ratio $\mathcal{B}(\mu N \to eN)/\mathcal{B}(\mu \to e\gamma)$ from the $g_{\mu R(L)}g_{eL(R)}$ term is enhanced and different from case I.

We see in Fig. 8 that parameters with δ_{RL} [as shown in (c) and (d)] are most constrained by data. It is likely that these parameters give dominant contributions to LFV processes. Using Figs. 9(c) and 9(d) we find that the present bound on $\mu \to e\gamma$ allows

$$\mathcal{B}(\mu N \to eN) \lesssim 10^{-13}, \tag{38}$$

which is close to the present bounds (see Table I). Therefore, the search on these processes could be very interesting.

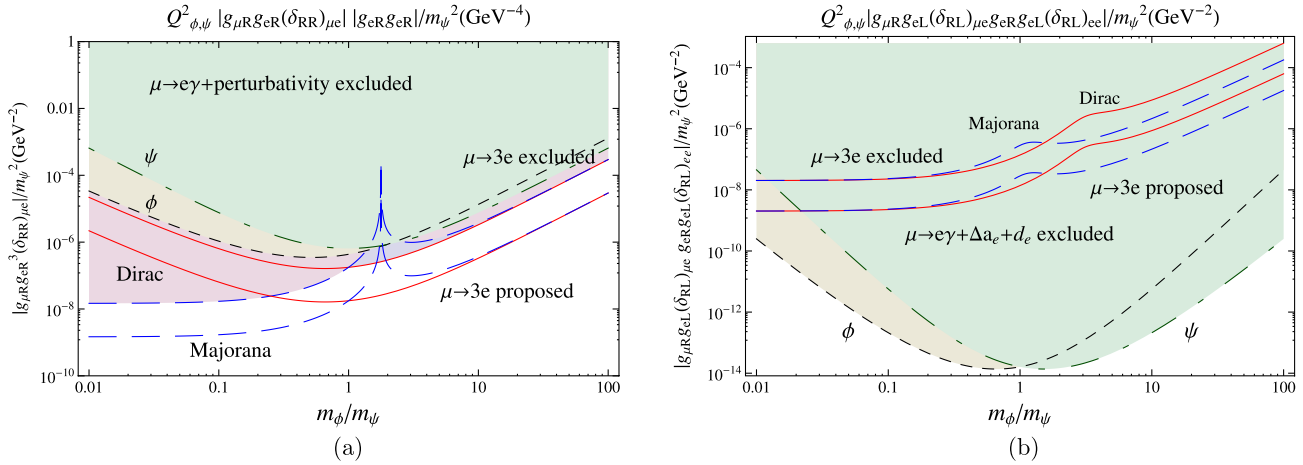

FIG. 10 (color online). Same as Fig. 6, but in case II.

In Fig. 10, we show the constraints on parameters that contribute through box diagrams to the $\mu^+ \to 3e$ process in this case. Although we also see some relaxations on parameters, the main conclusion remains similar to that in case I.

IV. DISCUSSION

A. Flavor violating Z decays

Lepton flavor violating $Z \to \mu^\mp e^\pm$ decays are highly related to $\mu \to 3e$, $\mu \to e\gamma$ and $\mu N \to eN$ processes via the Z-penguin contributions. The $Z \to l'\bar{l}$ decay rate is given by

$$\Gamma(Z \to l'\bar{l}) = \frac{m_Z^5}{24\pi}(|g^Z_{L'L}|^2 + |g^Z_{R'R}|^2), \tag{39}$$

where the dimensionful coefficient $g^Z_{M'M}$ is the same one used in Eq. (12). Using Eq. (39) and the results in the previous section, we find that the present bounds from $\mu \to 3e$, $\mu\mathrm{Ti} \to e\mathrm{Ti}$, and $\mu\mathrm{Au} \to e\mathrm{Au}$ processes constrain

$$\mathcal{B}(Z \to \mu^\mp e^\pm) \le 4 \times 10^{-13}, \quad 7 \times 10^{-14}, \quad 6 \times 10^{-15}, \tag{40}$$

respectively. Note that the above equation holds in both case I and II. In any case, these constraints are far below the present limit, $\mathcal{B}(Z \to \mu^\mp e^\pm) \le 1.7 \times 10^{-6}$.

B. Box diagrams involving quarks

From the explicit assignment of gauge quantum numbers of ψ and ϕ as shown in Appendix A, we see that it is possible to have ϕ couples to quarks [see Eq. (A5)]. These interactions can generate additional contributions to $\mu N \to eN$ conversion precesses through box diagrams similar to those in the $\mu \to 3e$ ones as shown in Figs. 1(c) and 1(d), but with the (lower) electron line replaced by a quark line.

To have interaction with quarks, only rather specific choices of ψ and ϕ gauge quantum numbers are allowed (see Appendix A). In particular, the case of ψ_R: $(1, 1, 1)$ and ϕ_L: $(1, 2, -1/2)$ are of interest, for the fermion field is a SM singlet. Below, we will use this case to illustrate the contributions from the additional box diagrams.

The interacting Lagrangian in this case is

$$\mathcal{L}_{\mathrm{int}} = g_{lL}\bar{\psi}_R L_{L_i}\phi^*_{Li} + g_u\bar{Q}_{Li}u_R\phi_{L_i} + g_d\bar{Q}_{Li}d_R\epsilon_{ij}\phi^*_{Lj} + \mathrm{H.c.}, \tag{41}$$

where Q_L and L_L are the quark and lepton doublets, respectively. Note that only the lower components of L_L and ϕ_L are relevant to this analysis. The box diagrams give

$$g_{RV}(q) = 0, \qquad g_{LV}(d) = 0 \tag{42}$$

and

$$g_{LV}(u) = \frac{1}{16\pi^2}\left\{-\frac{1}{8}G(m_\psi^2, 0, m_\phi^2, m_\phi^2)(g^*_{eL}g_{\mu L}) \times (g^*_u g_u + g^*_d g_d)\right\}, \tag{43}$$

where quark masses have been neglected. Note that the box diagrams also give the so-called $g_{LP}(u)$ term, which, however, does not contribute to conversion rates [10]. The resulting $\mu N \to eN$ conversion rates can be calculated using Eq. (18).

Experimental limits on conversion rates are used to constrain couplings and masses. The result is shown in Fig. 11. The correlation between $\mu N \to eN$ conversions and the $\mu^+ \to 3e$ decay are lost. In fact, we see that the constraints on $|g_{\mu L}g_{eL}|(|g_u|^2 + |g_d|^2)/m^2_\psi$ from present limits on $\mu \to e$ conversion rates are similar to the constraints on $|g_{\mu L}g_{eL}||g_{eL}g_{eL}|/m^2_\psi$ from the $\mu^+ \to 3e$ bound (see Fig. 6). Therefore, we may be able to see $\mu N \to eN$ conversions sooner than the $\mu^+ \to 3e$ decay, if $g_{u,d}$ is larger than g_{eL} and vice versa. The $\mu N \to eN$ conversion rates need not be highly suppressed as noted in Sec. III A.

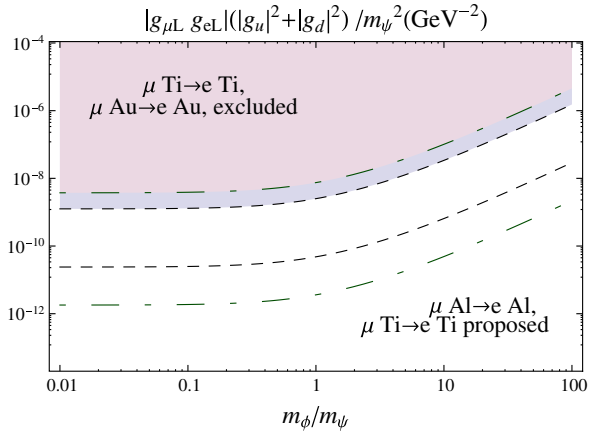

FIG. 11 (color online). Allowed parameter space for $|g_{\mu L} g_{eL}|^2(|g_u|^2 + |g_d|^2)/m_\psi^2$ constrained by $\mu \to e$ conversion data. Note that dot-dashed and short-dashed lines denote constraints from $\mu\mathrm{Ti} \to e\mathrm{Ti}$ and $\mu\mathrm{Au(Al)} \to e\mathrm{Au(Al)}$ conversion bounds, respectively.

C. Some other cases

A similar analysis can be preformed by replacing the spin-0 particle with a spin-1 particle in the loops. It will be interesting to compare it to the present work. However, gauge-invariant and triplet vector couplings will complicate the analysis. The study will be given elsewhere.

We expect to find results similar to those in case II, but with cancellation at work in the low m_ψ region if we introduce the built-in cancellation mechanism in the ψ sector instead of in the ϕ sector.

V. CONCLUSIONS

In conclusion, we use a model-independent approach in this analysis, where these processes are considered to be loop induced by exchanging spin-1/2 and spin-0 particles. We explore two complementary cases, which have no cancellation mechanism in amplitudes or an internal (built-in) cancellation mechanism. Our main results are as follows:

(a) Bounds from rates are used to constrain parameters, such as coupling constants and masses. These constraints can be easily updated by simple scalings, if the experimental situations change.
(b) The muon $g-2$ data favor nonchiral interactions.
(c) In $\mu^+ \to e^+e^-e^-$ and $\mu^- N \to e^- N$ processes, the Z-penguin diagrams may play some role, while the box diagram contributions to the $\mu^+ \to e^+e^-e^-$ rate are usual highly constrained.
(d) Z-penguin contributions can be constrained from $\mu^+ \to e^+\gamma$ and $\mu^- N \to e^- N$ bounds. It can then be used to constrain the $Z \to e^{\mp}\mu^{\pm}$ rate by seven to eight orders of magnitude lower than the present experimental bound.
(e) In the first case (without any built-in cancellation mechanism), using the recent $\mu^+ \to e^+\gamma$ bound, we find that $\mu^+ \to e^+e^-e^-$ and $\mu^- N \to e^- N$ rates are bounded below the present experimental limits by two to three orders of magnitude in general. In some cases, the above expectation on low $\mu^- N \to e^- N$ rates can be relaxed, as additional box diagrams involving quarks contribute to $\mu^- N \to e^- N$ processes.
(f) Furthermore, by comparing Δa_μ and $\mathcal{B}(\mu \to e\gamma)$ data, the couplings of g_μ and g_e are found to be highly hierarchical [see Eq. (35)]. Additional suppression mechanisms should be called for.
(g) In the second case (with a built-in cancellation mechanism), mixing angles can provide additional suppression factors to satisfy the Δa_μ and $\mathcal{B}(\mu \to e\gamma)$ bounds without relay only on highly hierarchical g_e and g_μ couplings.
(h) In addition, although the $\mu^+ \to e^+e^-e^-$ rate remains suppressed, the bounds on $\mu^- N \to e^- N$ rates, implicated from the MEG $\mu^+ \to e^+\gamma$ bound, can be relaxed significantly in the second case and can be just below the present experimental limits.

ACKNOWLEDGMENTS

This research was supported in part by the National Science Council of R.O.C. under Grant Nos. NSC97-2112-M-033-002-MY3 and No. NSC100-2112-M-033-001-MY3.

APPENDIX A: GAUGE QUANTUM NUMBERS OF ϕ AND ψ

The $\psi - \phi - l$ Lagrangian,

$$\mathcal{L}_{\mathrm{int}} = g'_L(\bar{\psi}_R\phi^*_L)_i(L_L)_i + g'_R\bar{\psi}_L\phi^*_R l_R + \mathrm{H.c.}, \qquad \text{(A1)}$$

where i is the weak isospin index, is gauge invariant under the SM gauge transformation. Recall that the lepton quantum numbers under SU(3) × SU(2) × U(1) are given by

$$L_L\colon \left(1, 2, -\frac{1}{2}\right), \qquad l_R\colon (1, 1, -1). \qquad \text{(A2)}$$

The gauge-invariant requirement implies that we must have the following quantum number assignments for these combinations:

$$\bar{\psi}_R\phi^*_L\colon \left(1, 2, \frac{1}{2}\right), \qquad \bar{\psi}_L\phi^*_R\colon (1, 1, 1). \qquad \text{(A3)}$$

Consequently, the gauge quantum numbers of ψ and ϕ are related as follows:

$$\begin{aligned} &\psi_R\colon (c_R, 2I_R + 1, Y_R),\\ &\phi_L\colon \left(\bar{c}_R, 2\left(I_R \pm \frac{1}{2}\right) + 1, Y_R - \frac{1}{2}\right),\\ &\psi_L\colon (c_L, 2I_L + 1, Y_L), \qquad \phi_R\colon (\bar{c}_L, 2I_L + 1, Y_R - 1). \end{aligned} \qquad \text{(A4)}$$

Some examples for the assignments of the quantum numbers of $\psi_{L,R}$ and $\phi_{L,R}$ are given in Table II.

Note that in the cases of $I_R = 0$, $Y_R = 0$ and $I_L = 1/2$, $Y_L = 1/2$, ϕ_L and ϕ_R can couple to quarks, respectively, through

TABLE II. Some examples for the assignment of the quantum numbers of $\psi_{L,R}$ and $\phi_{L,R}$.

ψ_R	ϕ_L	ψ_L	ϕ_R
$(1, 1, Y_R)$	$(1, 2, Y_R - \frac{1}{2})$	$(1, 1, Y_L)$	$(1, 1, Y_L - 1)$
$(1, 2, Y_R)$	$(1, 1, Y_R - \frac{1}{2})$	$(1, 2, Y_L)$	$(1, 2, Y_L - 1)$
$(3(\bar{3}), 1, Y_R)$	$(\bar{3}(3), 2, Y_R - \frac{1}{2})$	$(3(\bar{3}), 1, Y_L)$	$(\bar{3}(3), 1, Y_L - 1)$
$(3(\bar{3}), 2, Y_R)$	$(\bar{3}(3), 1, Y_R - \frac{1}{2})$	$(3(\bar{3}), 2, Y_L)$	$(\bar{3}(3), 2, Y_L - 1)$

TABLE III. Parameters of overlap integrates and total capture rates $\omega_{\rm capt}$ taken from Refs. [10,11].

	$D(m_\mu^{5/2})$	$V^{(p)}(m_\mu^{5/2})$	$V^{(n)}(m_\mu^{5/2})$	$\omega_{\rm capt}(10^6\ {\rm s}^{-1})$
$^{27}_{13}$Al	0.0362	0.0161	0.0173	0.7054
$^{48}_{22}$Ti	0.0864	0.0396	0.0468	2.59
$^{197}_{79}$Au	0.189	0.0974	0.146	13.07
$^{205}_{81}$Tl	0.161	0.0834	0.128	13.90

$$\bar{Q}_{Li} u_R \phi_{Li}, \qquad \bar{Q}_{Li} d_R \phi_{Ri}, \qquad \bar{Q}_{L_i} u_R \epsilon_{ij} \phi^\dagger_{Rj}, \qquad \bar{Q}_{L_i} d_R \epsilon_{ij} \phi^\dagger_{Lj}, \tag{A5}$$

where ϵ_{ij} is the antisymmetric tensor. It is easy to see that the above terms are indeed gauge invariant by using $\bar{Q}_L q_R$: $(1, 2, -1/6 + Q_q)$ and Eq. (A4).

APPENDIX B: LOOP FUNCTIONS AND INPUT PARAMETERS

The loop functions used in this work are defined as

$$\begin{aligned}
F_1(a,b) &= \frac{1}{12(a-b)^4}\left(2a^3 + 3a^2 b - 6ab^2 + b^3 + 6a^2 b \ln\frac{b}{a}\right),\\
F_2(a,b) &= \frac{1}{2(a-b)^3}\left(-3a^2 + 4ab - b^2 - 2a^2 \ln\frac{b}{a}\right),\\
F_3(a,b) &= \frac{1}{2(a-b)^3}\left(a^2 - b^2 + 2ab \ln\frac{b}{a}\right),\\
G_1(a,b) &= \frac{1}{36(a-b)^4}\left(-(a-b)(11a^2 - 7ab + 2b^2) - 6a^3 \ln\frac{b}{a}\right),\\
G_2(a,b) &= \frac{1}{36(a-b)^4}\left(-(a-b)(16a^2 - 29ab + 7b^2) - 6a^2(2a-3b) \ln\frac{b}{a}\right),\\
G_3(a,b) &= \frac{1}{36(a-b)^5}\left(-(a-b)(17a^2 + 8ab - b^2) - 6a^2(a+3b) \ln\frac{b}{a}\right),\\
F_Z(a_1,a_2,b,b,c) &= -\frac{a_1(2\sqrt{a_1 a_2} - a_1)}{2(a_1-a_2)(a_1-b)} \ln\frac{a_1}{c} + \frac{a_2(2\sqrt{a_1 a_2} - a_2)}{2(a_1-a_2)(a_2-b)} \ln\frac{a_2}{c} - \frac{b(2\sqrt{a_1 a_2} - b)}{2(a_1-b)(a_2-b)} \ln\frac{b}{c}\\
F_Z(a,a,b_1,b_2,c) &= -\frac{3}{4} + \frac{a^2}{2(a-b_1)(a-b_2)} \ln\frac{a}{c} - \frac{b_1^2}{2(a-b_1)(b_1-b_2)} \ln\frac{b_1}{c} + \frac{b_2^2}{2(a-b_2)(b_1-b_2)} \ln\frac{b_2}{c},\\
G_Z(a_1,a_2,b) &= \frac{a_1\sqrt{a_1 a_2}}{(a_1-a_2)(a_1-b)} \ln\frac{a_1}{b} - \frac{a_2\sqrt{a_1 a_2}}{(a_1-a_2)(a_2-b)} \ln\frac{a_2}{b},\\
F(a,b,c,d) &= \frac{b\sqrt{ab}}{(a-b)(b-c)(b-d)} \ln\frac{b}{a} - \frac{c\sqrt{ab}}{(a-c)(b-c)(c-d)} \ln\frac{c}{a} + \frac{d\sqrt{ab}}{(a-d)(b-d)(c-d)} \ln\frac{d}{a},\\
G(a,b,c,d) &= -\frac{b^2}{(a-b)(b-c)(b-d)} \ln\frac{b}{a} + \frac{c^2}{(a-c)(b-c)(c-d)} \ln\frac{c}{a} - \frac{d^2}{(a-d)(b-d)(c-d)} \ln\frac{d}{a}.
\end{aligned} \tag{B1}$$

Note that these loop functions are dimensionful, and the dimension of G_3 is different from others. We do not have the expression of $F_Z(a_1, a_2, b_1, b_2, c)$, since in Sec. II C only $a_1 = a_2 = a$ and/or $b_1 = b_2 = b$ are needed. Both expressions of F_Z give identical results in the $a_1 = a_2 = a$ and $b_1 = b_2 = b$ cases.

The numerical values of D, V, and $\omega_{\rm capt}$ used in Eq. (18) are collected in Table III.

[1] J. Adam *et al.* (MEG Collaboration), Phys. Rev. Lett. **107**, 171801 (2011).
[2] K. Nakamura *et al.* (Particle Data Group Collaboration), J. Phys. G **37**, 075021 (2010).
[3] H. K. Dreiner, K. Nickel, F. Staub, and A. Vicente, Phys. Rev. D **86**,, 015003 (2012); J. Chakrabortty, P. Ghosh, and W. Rodejohann, arXiv:1204.1000; G. Blankenburg, G. Isidori, and J. Jones-Perez, Eur. Phys. J. C **72**, 2126 (2012); D. Grossman and Y. Nir, Phys. Rev. D **85**, 055004 (2012).
[4] L. Calibbi, Z. Lalak, S. Pokorski, and R. Ziegler, J. High Energy Phys. 07 (2012) 004; S. Davidson, Eur. Phys. J. C **72**, 1897 (2012).
[5] X.-G. He and S. K. Majee, J. High Energy Phys. 03 (2012) 023; A. Goudelis, O. Lebedev, and J.-h. Park, Phys. Lett. B **707**, 369 (2012); C.-W. Chiang, Y.-F. Lin, and J. Tandean, J. High Energy Phys. 11 (2011) 083.
[6] Y. Kuno and Y. Okada, Rev. Mod. Phys. **73**, 151 (2001).
[7] Y. Kuno, Contribution to the Flavor Physics and *CP* Violation Conference 2010, Turin, Italy (unpublished); Proc. Sci., FPCP (2010) 049;M. De Gerone and (MEG Collaboration), arXiv:1108.2670; T. Nomura, Contribution to the Flavor Physics and *CP* Violation Conference, 2011, Maale HaChamisha, Israel (unpublished); B. Casey, *ibid.*; A. Hoecker, arXiv:1201.5093.
[8] F. Jegerlehner and A. Nyffeler, Phys. Rep. **477**, 1 (2009).
[9] G. Dissertori, Contribution to the Moriond QCD and High Energy Interactions Conference, 2012, La Thuile, Aosta Valley, Italy (unpublished); R. Barbieri, Contribution to the 36th International Conference on High Energy Physics, 2012, Melbourne, Australia (unpublished).
[10] R. Kitano, M. Koike, and Y. Okada, Phys. Rev. D **66**, 096002 (2002); **76**, 059902(E) (2007).
[11] T. Suzuki, D. F. Measday, and J. P. Roalsvig, Phys. Rev. C **35**, 2212 (1987).
[12] F. Gabbiani, E. Gabrielli, A. Masiero, and L. Silvestrini, Nucl. Phys. **B477**, 321 (1996).
[13] Y. K. Semertzidis, H. Brown, G. T. Danby, J. W. Jackson, R. Larsen, D. M. Lazarus, W. Meng, W. M. Morse *et al.*, arXiv:hep-ph/0012087.
[14] M. Hirsch, F. Staub, and A. Vicente, Phys. Rev. D **85**, 113013 (2012).